nature chemistry

ARTICLES

https://doi.org/10.1038/s41557-020-00595-w

Isolation and electronic structures of derivatized manganocene, ferrocene and cobaltocene anions

Conrad A. P. Goodwin[1,2], Marcus J. Giansiracusa[1], Samuel M. Greer[2,3,4], Hannah M. Nicholas[1], Peter Evans[1], Michele Vonci[1], Stephen Hill[3,5], Nicholas F. Chilton[1]✉ and David P. Mills[1]✉

The discovery of ferrocene nearly 70 years ago marked the genesis of metallocene chemistry. Although the ferrocenium cation was discovered soon afterwards, a derivatized ferrocenium dication was only isolated in 2016 and the monoanion of ferrocene has only been observed in low-temperature electrochemical studies. Here we report the isolation of a derivatized ferrocene anion in the solid state as part of an isostructural family of 3*d* metallocenates, which consist of anionic complexes of a metal centre (manganese, iron or cobalt) sandwiched between two bulky Cp^{ttt} ligands (where Cp^{ttt} is {1,2,4-C_5H_2 $^tBu_3$}). These thermally and air-sensitive complexes decompose rapidly above −30 °C; however, we were able to characterize all metallocenates by a wide range of physical techniques and ab initio calculations. These data have allowed us to map the electronic structures of this metallocenate family, including an unexpected high-spin *S* = 3/2 ground state for the 19e$^-$ derivatized ferrocene anion.

The iconic organometallic complex ferrocene, [Cp_2Fe] (FcH, Cp = cyclopentadienyl, η^5-C_5H_5), was first reported in 1951[1,2], and the ferrocenium cation, [Cp_2Fe]$^+$ (FcH$^+$), was isolated soon after[3]. These discoveries were the harbingers of metallocene chemistry, which rapidly spread to cover most of the periodic table[4,5]. In the interim, ferrocene has become a versatile workhorse in nanotechnology[6], electrochemistry, catalysis, medicine and functional materials[7], with industrial applications including fuel additives and the synthesis of agrochemicals and pharmaceuticals[8]. A defining feature of ferrocene is its facile oxidation to ferrocenium, with the fully reversible FcH$^{+/0}$ redox couple being a standard reference in non-aqueous electrochemical processes[9].

Although metallocenes are strictly defined as the homoleptic [Cp_2M] family, Cp derivatization to Cp^R ligands ($C_5R_nH_{5-n}^-$) provides tunable physicochemical properties[4,5]; for example, decamethylferrocene, [Cp^*_2Fe] (Cp* = C_5Me_5), can be doubly oxidized to yield dicationic [Cp^*_2Fe]$^{2+}$ salts[10]. Isolated metallocene anions are conspicuous by their absence in the literature, with '[Cp_2M]$^-$' (M = V[11], Cr[11], Fe[12,13], Co[14,15], Ni[11]) and '[Cp_2M]$^{2-}$' (M = Co, Ni)[15] anions only identified as transient species in seminal low-temperature solution-phase electrochemical studies. Notable synthetic results include the reduction of [Cp^*_2Mn] to an orange powder formulated as 'Na[Cp^*_2Mn]'[16,17], the preparation of white powders of 'A[Cp_2Re]' (A = Li[18], K[19]) from [Cp_2ReH] and ^{n}BuLi or $PhCH_2K$, and the structural characterization of a derivatized bis(indenyl) Co anion, [Na(THF)$_6$][Co{C_9H_5-1,3-($SiMe_3$)$_2$}$_2$][20]. Recently, potassium salts of [Cp^*_2Mn]$^-$ were structurally authenticated[21]. It was previously shown that replacement of a Cp^R ligand with an arene (C_6R_6) can provide neutral 19e$^-$ mixed sandwich Fe complexes. Some of the [(Cp^R)Fe(C_6Me_6)] family are stable at room temperature, allowing characterization by single-crystal X-ray diffraction (XRD)[22,23]. Finally, the related 19e$^-$ Fe bis-stannole complex [Li(THF)$_4$][Fe{$SnC_4(SiMe_3)_2$-1,3-Me_2-2,4}$_2$] was recently isolated and structurally authenticated[24].

In this Article, we report the isolation of an isostructural series of derivatized metallocene anions for Mn, Fe and Co. Despite their facile thermal decomposition above −30 °C, these complexes were characterized by a wide range of physical techniques. Together with ab initio calculations, these studies provide new insights into the electronic structures of metallocenes, including a 19e$^-$ Fe metallocene anion with a high-spin S = 3/2 ground state rather than the low-spin S = 1/2 ground state observed in formally isoelectronic cobaltocenes[4,5].

Results and discussion

Electrochemistry. We targeted [(Cp^{ttt})$_2$M]$^-$ (Cp^{ttt} = {1,2,4-$C_5H_2$$^tBu_3$}) anions, as the six bulky aliphatic ^{t}Bu substituents impart solubility and kinetic stability. [(Cp^{ttt})$_2$M] precursors are known for M = Mn (**1**)[25,26], Fe (**2**)[27] and Co (**3**)[28,29]. Here we prepared **3** from $CoCl_2$ and 2 equiv. of KCp^{ttt} (ref. [30]). We performed cyclic voltammetry on 1,2-dimethoxyethane (DME) solutions of **1**, **2** and **3** at −50 °C with [N^{n}Bu$_4$][BF_4] as the supporting electrolyte to determine reduction potentials and to assess metallocenate stabilities (Fig. 1). The quasi-reversible reduction processes ($\Delta E_{ox/red}$ (mV) = 760, **1**; 390, **2**; 270, **3**) are similar for **2** and **3**, whereas **1** shows evidence of reactivity on the experimental timescale at negative potentials ($E_{½}$ (V) versus FcH$^{+/0}$ = −3.39, **2**; −2.49, **3**; for **1** E_{p1} = −3.26 V and E_{p2} = −2.50 V at peak current density). These reduction waves are all irreversible above −30 °C and are formally assigned as M^{2+}/M^{1+} processes from their similarity to the respective voltammograms of [Cp_2M] (M = Fe, −3.45 to −3.57 V; Co, −2.40 to −2.55 V; versus FcH$^{+/0}$)[12–15] and [Cp^*_2Mn] (−2.68 V; versus FcH$^{+/0}$)[16]. Note that, for **1**, we cannot definitively assign if E_{p1} and E_{p2} belong to the same redox couple.

Synthesis. Given the large negative reduction potentials and temperature sensitivity seen in electrochemical studies, we reasoned that low-temperature alkali metal reductions would be required to isolate 3*d* metallocenates. Such conditions previously opened up elusive formal +2 oxidation states for *f*-element Cp^R complexes[31].

[1]Department of Chemistry, School of Natural Sciences, The University of Manchester, Manchester, UK. [2]Chemistry Division, Los Alamos National Laboratory, Los Alamos, NM, USA. [3]National High Magnetic Field Laboratory, Florida State University, Tallahassee, FL, USA. [4]Department of Chemistry & Biochemistry, Florida State University, Tallahassee, FL, USA. [5]Department of Physics, Florida State University, Tallahassee, FL, USA. ✉e-mail: nicholas.chilton@manchester.ac.uk; david.mills@manchester.ac.uk

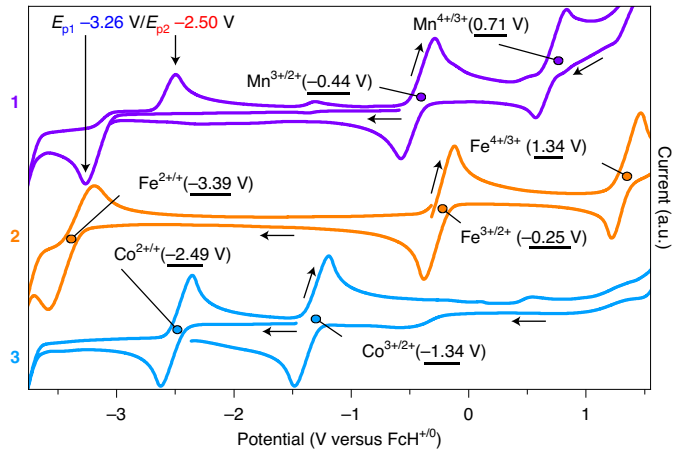

Potential (V versus $FcH^{+/0}$)	**1** (Mn)	**2** (Fe)	**3** (Co)
$[(Cp^{ttt})_2M]^{0/-}$ ($M^{2+/+}$)	NA	–3.39	–2.49
$[(Cp^{ttt})_2M]^{+/0}$ ($M^{3+/2+}$)	–0.44	–0.25	–1.34
$[(Cp^{ttt})_2M]^{2+/+}$ ($M^{4+/3+}$)	0.71	1.34	NA

Fig. 1 | Electrochemical studies for 1, 2 and 3. Cyclic voltammograms (current in arbitrary units (a.u.) versus potential in V versus $FcH^{+/0}$) of **1** (Mn, purple), **2** (Fe, orange) and **3** (Co, blue) at −50 °C, 1 mM in DME with 0.5 M $[N^nBu_4][BF_4]$ (**1** and **3**, 200 mV s^{-1}; **2**, 100 mV s^{-1}), with redox processes labelled with formal metal oxidation states and arrows to indicate the scan direction. As the formal $Mn^{2+/+}$ redox couple of **1** is not reversible, the peak potentials are denoted (E_{p1}/E_{p2}) at the point of peak current density. The table compiles half-wave ($E_{1/2}$) or peak potential values (V versus $FcH^{+/0}$) for the electrochemical redox processes $[(Cp^{ttt})_2M]^{0/-}$, $[(Cp^{ttt})_2M]^{+/0}$ and $[(Cp^{ttt})_2M]^{2+/+}$ for complexes **1**, **2** and **3** when observed.

Thus, potassium graphite (KC_8) reductions of **1**, **2** and **3** in tetrahydrofuran (THF) at −40 °C, in the presence of 2.2.2-cryptand to sequester potassium cations, gave the substituted metallocenates, [K(2.2.2-cryptand)][$(Cp^{ttt})_2$M] (M = Mn, **4**; Fe, **5**; Co, **6**) (Fig. 2). Complex **4** reproducibly co-crystallized with 1 equiv. of [K(2.2.2-cryptand)][Cp^{ttt}], and thus is formally **4·K(2.2.2-cryptand)Cp^{ttt}**. An analogous contaminant, [K(2.2.2-crypt)]$_2$[$(Cp^{ttt})_2$Co][Cp^{ttt}] (**7**), was sometimes observed in batches of **6**. The formulations of **4**, **5** and **6** were consistent with values obtained from elemental microanalysis, indicating that the single-crystal XRD data are representative of the bulk samples. Intensely coloured THF or DME solutions of **4** (orange), **5** (brown) and **6** (brown) at room temperature change colour within 10 min and crystals of **1**, **2** and **3** were isolated from the resultant mixtures, thus all analytical data for **4**, **5** and **6** were collected below −30 °C. Surprisingly the 18e^- complex **4** is the most thermally sensitive of the series; this is in stark contrast to the derivatized manganocene anion $[Cp^*_2Mn]^-$, which has recently been synthesized by refluxing $[Cp^*_2Mn]$ with molten K in THF[21]. This temperature sensitivity precluded the collection of reliable magnetic and NMR spectroscopic data for **4**, **5** and **6** despite multiple attempts, but otherwise we were able to fully characterize this family.

Structural characterization. The solid-state structures of **1**–**7** and [K(2.2.2-crypt)][Cp^{ttt}] (**8**) were determined by single-crystal XRD at 150 K. As the $[(Cp^{ttt})_2M]$ fragments are structurally analogous, only the structure of **5** is depicted in Fig. 2, and selected bond lengths and angles are compiled in Table 1. The structures of **1**, **2** and **3** have been reported previously[25–27,29]. In common with these[25–27,29], near-eclipsed conformations of the C_5 rings are observed for **4**–**7**, with the quaternary carbons of the ^{t}Bu groups displaced from the Cp^{ttt} C_5 planes away from the metal due to steric crowding. This also causes all the $Cp^{ttt}_{centroid}$···M···$Cp^{ttt}_{centroid}$ angles to deviate from linearity, with **5** exhibiting the most bent geometry at 169.38(11)°; in contrast to **4**–**6**, [K(18-crown-6)$(THF)_2$][Cp^*_2Mn] exhibits a highly axial geometry ($Cp^*_{centroid}$···Mn···$Cp^*_{centroid}$: 179.5(2)°)[21]. The M–C_{Cp} and M···$Cp^{ttt}_{centroid}$ distances for **1**–**7** approximately correlate with valence electron counts, with the shortest values seen for the 18e^- **2** and **4** and longer distances for the 19e^- **3** and **5** and 20e^- **6** and **7**, presumably due to the partial occupancy of antibonding orbitals. As expected, these bond distances increase upon reduction of **2** to **5** and from **3** to **6** or **7**. The seemingly anomalous long distances for the 17e^- **1** are due to its high-spin configuration, which results in significant electron density in antibonding orbitals[26]. The mean Mn···$Cp^{ttt}_{centroid}$ distances for **4** (1.750(3) Å) are longer than the corresponding distances in [K(18-crown-6)$(THF)_2$][Cp^*_2Mn] (mean M···$Cp^*_{centroid}$: 1.673(7) Å)[21] due to the greater steric bulk of Cp^{ttt} versus Cp^*. The 19e^- **5** exhibits longer M···$Cp^{ttt}_{centroid}$ distances than seen for the 19e^- **3** and 20e^- **6** and **7**, motivating us to analyse their electronic structures.

Ab initio electronic structure. Given that $[Cp_2Mn]$ is high-spin[32,33], but becomes low-spin below 100 K when doped into a diamagnetic matrix of $[Cp_2Fe]$[34], and that $[Cp^*_2Mn]$ is low-spin[16], it is evident that electron–electron repulsion and crystal field effects in 3*d* metallocenes have similar energy scales. Indeed, at room temperature, 1,1′-dimethylmanganocene shows evidence of both a sextet and doublet ground state[35]. A multiconfigurational wavefunction-based method accounting for electron correlation is therefore the only reliable way of treating the electronic structure, so we performed state-average complete active space self-consistent field (SA-CASSCF) calculations, with spin–orbit coupling (SOC) included a posteriori, as embodied by the OpenMOLCAS code[36]. For **2**–**7** the active space consisted of 12 orbitals ($3d_{xz}$ and $3d_{yz}$ (π, e_{1g}), $3d_{z^2}$ (σ, a_{1g}), $3d_{xy}$ and $3d_{x^2-y^2}$ (δ, e_{2g}), and $3d_{xz}$ and $3d_{yz}$ (π^*, e_{1g}) and ligand-hybridized 4*d*/5*d* orbitals), while for **1** this active space was not stable and our calculations only included five orbitals ($3d_{z^2}$ (σ, a_{1g}), $3d_{xy}$ and $3d_{x^2-y^2}$ (δ, e_{2g}), and $3d_{xz}$ and $3d_{yz}$ (π^*, e_{1g})). Here we focus on the metallocenates **4**–**7** (a discussion of **1**–**3** is provided in the Supplementary Information).

For **4**, using an active space of 10 electrons in 12 orbitals (CAS(10,12) + SO, complete active space, + spin-orbit, Supplementary Table 13), the ground state is low-spin S = 0 (^{1}A), with a first excited S = 1 state lying at ~15,000 cm^{-1}. Thus, these calculations suggest that **4** is low-spin diamagnetic, just like its isoelectronic partner **2**. For **5**, using CAS(11,12) + SO (Supplementary Table 15) the ground state was found to be high-spin S = 3/2 (^{4}E), but, due to the low symmetry of the molecule, the orbital degeneracy of the $3d_{xy}$ and $3d_{x^2-y^2}$ pair is partly lifted, thus the ^{4}E is split into two S = 3/2 states separated by ~1,100 cm^{-1} (subsequent excited states, ~10,000 cm^{-1}). The ground S = 3/2 state has very large zero-field splitting that can be parameterized by $D = -36.4\ cm^{-1}$ and $|E| = 0.15\ cm^{-1}$, where D and E are the axial and rhombic second-order zero-field splitting parameters, respectively, meaning that the lowest-lying Kramers doublet is $m_S = \pm 3/2$, with the $m_S \pm 1/2$ doublet lying at 72.8 cm^{-1}. The g value for the ground state is also anisotropic, with $g_x = g_y = 2.02$ and $g_z = 2.72$, leading to effective g values for the ground Kramers doublet of $g_x = g_y = 0.02$ and $g_z = 8.11$, while those for the first excited doublet are $g_x = g_y = 4.02(3)$ (value in parentheses is standard deviation of the average value) and $g_z = 2.82$. The magnetic z axis is parallel to the $Cp^{ttt}_{centroid}$···Fe···$Cp^{ttt}_{centroid}$ vector. Thus, **5** is rather different to its isoelectronic partner **3**, which is S = 1/2 (^{2}E). Finally, for the Co metallocenate there are two crystal structures, so calculations were performed on both; the first values are for **6** and those in braces are for **7**. Using a CAS(12,12) + SO calculation (Supplementary Tables 17 and 18) the ground state was found to be high-spin S = 1 (^{3}A), with a set

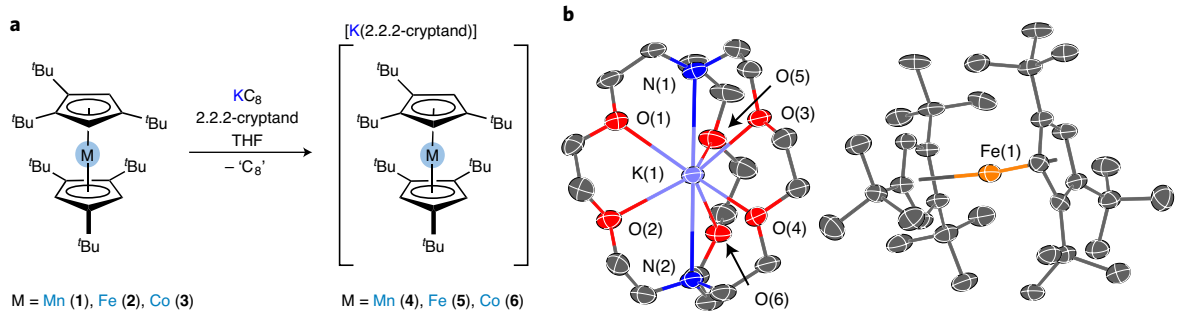

Fig. 2 | Synthesis of 4, 5 and 6 and molecular structure of 5. a, Synthesis of complexes **4**, **5** and **6**. **b**, Molecular structure of **5**, with selective atom labelling (Fe, orange; K, violet; O, red; N, blue; C, grey). Displacement ellipsoids are set at the 50% probability level and hydrogen atoms are omitted for clarity.

Table 1 | Selected distances (Å) and angles (°) for 1–7 (data for 1–3 agree with refs. [25,27,29])

Complex	Range M–C_{Cp}	Mean M···$Cp^{ttt}_{centroid}$	$Cp^{ttt}_{centroid1}$···M···$Cp^{ttt}_{centroid2}$	Formal e^- count
1	2.347(2)–2.516(2)	2.105(2)	169.63(3)	17
2	2.034(3)–2.156(3)	1.715(2)	174.91(8)	18
3	2.121(2)–2.227(2)	1.802(2)	174.77(4)	19
4	2.099(4)–2.159(4)	1.750(3)	174.68(9)	18
5	2.262(5)–2.511(6)	2.064(4)	169.38(11)	19
6	2.220(3)–2.451(3)	1.958(2)	175.96(5)	20
7	2.225(2)–2.415(2)	1.930(2)	176.20(5)	20

of four excited S = 1 states lying between 11,000 and 12,000 cm^{-1} {12,000–13,000 cm^{-1}}, and has a sizable zero-field splitting that can be parameterized by $D = +25.6\,cm^{-1}$ and $|E| = 0.21\,cm^{-1}$ {$D = +23.6\,cm^{-1}$ and $|E| = 0.41\,cm^{-1}$}, meaning that the lowest-lying state is $m_S = 0$ with the $m_S \pm 1$ pseudo-doublet lying at 24–26 cm^{-1}, with an intra-doublet separation of 0.4–0.8 cm^{-1}. The g value for the ground S = 1 state is anisotropic, with $g_x = g_y = 2.17(1)$ and $g_z = 2.00$ {$g_x = g_y = 2.15(1)$ and $g_z = 2.00$}, where the magnetic z axis is parallel to the $Cp^{ttt}_{centroid}$···Co···$Cp^{ttt}_{centroid}$ vector.

Mössbauer spectroscopy. Complexes **2** and **5** were studied by ^{57}Fe Mössbauer spectroscopy (Fig. 3, Supplementary Fig. 68 and Supplementary Table 19). The spectrum of **2** recorded at 80 K consists of a single quadrupole doublet that is best fit with an isomer shift of $\delta = 0.66(2)\,mm\,s^{-1}$ and a quadrupole splitting of $\Delta E_Q = 2.60(2)\,mm\,s^{-1}$ (Fig. 3a). The spectrum of **5** displays two quadrupole doublets, unambiguously indicating that two Fe species are present in this sample. The first species is described by parameters identical to those of **2**, so we assign this doublet to the presence of **2**, which forms upon thermal decomposition of **5** during sample preparation. The second species, which we attribute to **5**, features an asymmetric quadrupole doublet and is fit with $\delta = 1.25(2)\,mm\,s^{-1}$ and $\Delta E_Q = 1.23(2)\,mm\,s^{-1}$ (Fig. 3b). The observation of an asymmetric quadrupole doublet is common for Kramers systems, like **5**, in a slow to intermediate relaxation regime; that is, the relaxation rate is around the same order of magnitude as the ^{57}Fe Larmor precession (see Supplementary Information for further discussion)[37,38].

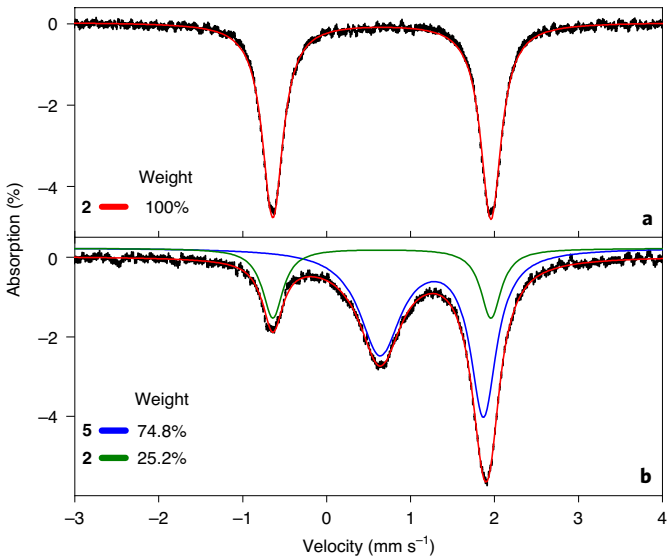

Sample/site	δ (mm s^{-1})	ΔE_Q (mm s^{-1})	Γ_L	Γ_R
2/N	0.66(2)	2.60(2)	0.3	0.3
5/A	1.25(2)	1.23(2)	0.6	0.38
5/N	0.66(2)	2.60(2)	0.3	0.3

Fig. 3 | Zero-field ^{57}Fe Mössbauer spectra for 2 and 5. a,**b**, ^{57}Fe Mössbauer spectra of powders recorded under zero applied magnetic field and 80 K (% absorption versus velocity, in mm s^{-1}) for a sample of $[(Cp^{ttt})_2Fe]$ (**2**) (experimental, black; simulated, red) (**a**) and a sample of $[K(2.2.2\text{-cryptand})][(Cp^{ttt})_2Fe]$ (**5**) (**b**), where the blue trace corresponds to the quadrupole doublet assigned to **5** (~75%) and the green trace originates from the presence of **2**, which forms upon the thermal decomposition of **5** (~25%). The red trace is the weighted sum of the two sub-spectra. The table compiles the experimentally determined ^{57}Fe Mössbauer parameters for the sites (independent Fe environments) in the two samples **2** and **5**, with N referring to the parameters of the neutral molecule $[(Cp^{ttt})_2Fe]$ and A to the anion, $[(Cp^{ttt})_2Fe]^-$. The following parameters are shown: δ, the isomer shift; ΔE_Q, the quadrupole splitting; Γ_L and Γ_R, the line widths at half maximum showing the asymmetry of the doublet for **5**. The numbers in parentheses indicate the estimated uncertainty in the last digit.

The isomer shift quantifies the electron density at the ^{57}Fe nuclei, and hence can be used to identify the oxidation state. Unfortunately, the isomer shifts in ferrocene ($\delta \approx 0.45$–0.6)[39,40] and the associated cations ($\delta \approx 0.51$–0.62 for 1+ (ref. [41]) and $\delta \approx 0.59\,mm\,s^{-1}$ for 2+ (ref. [10])) are similar. The isomer shift ranges of previously reported formally Fe^{1+} sandwich complexes (~0.52–0.73 at 77 K)[23,24,38,42] are

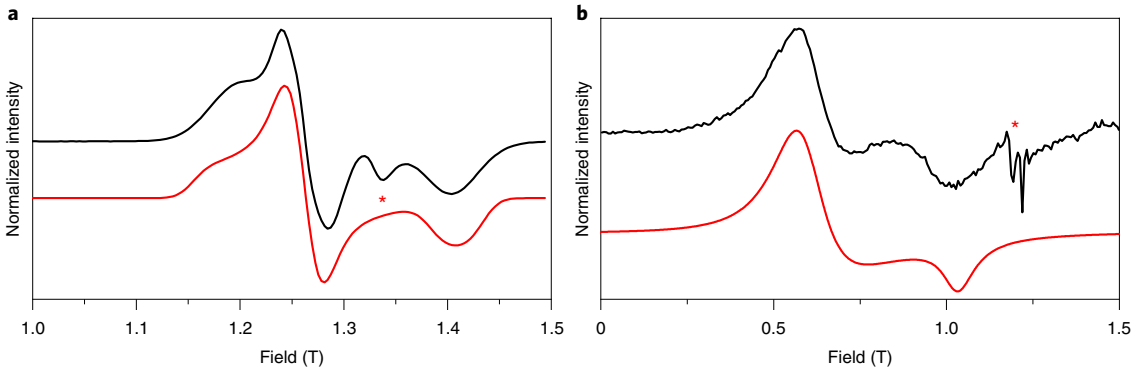

Fig. 4 | Continuous-wave Q-band EPR spectra of 3 and 5. a, Spectrum for **3** at 11 K (33.950645 GHz, red line is a simulation with $S=1/2$, $g_x=2.00$, $g_y=1.93$ and $g_z=1.72$, with $A_x=400$, $A_y=0$ and $A_z=150$ MHz and $lw_{iso}=30$ mT using Easyspin[41]). **b**, Spectrum for **5** at 5 K (34.080627 GHz, red line is a simulation with $S=3/2$, $D=-4.42\,cm^{-1}$ with $E=0\,cm^{-1}$ and $g_{x/y}=2.06$ and $g_z=2.37$, $lw_{x/y}=12.9$ and $lw_z=3.7$ GHz using PHI[42]). Asterisks denote extrinsic peaks. The resonances observed for **5** are at different magnetic fields to those seen for **3**, consistent with an assignment of **5** having an $S=3/2$ spin state.

smaller than that observed for **5**, but these literature examples almost exclusively exhibit low-spin ground states. Herein, we propose that **5** has a formal $4s^0 3d^7$ high-spin ground state with a reduced Fe spin population of +2.82 (see below).

To rationalize the unusually large isomer shift, we performed density functional theory (DFT) calculations with hybrid (B3LYP) and GGA (BP86) functionals (Supplementary Table 20). The calculated isomer shifts and quadrupole splitting parameters of **2** ($\delta^{calc}=0.61$–$0.69\,mm\,s^{-1}$, $|\Delta E_Q{}^{calc}|=2.51$–$3.37\,mm\,s^{-1}$) are in excellent agreement with the experimental values ($\delta=0.66(2)\,mm\,s^{-1}$, $|\Delta E_Q|=2.60(2)\,mm\,s^{-1}$). In the case of **5**, the calculated isomer shift for the high ($\delta^{calc}=1.09$–$1.27\,mm\,s^{-1}$) and low ($\delta^{calc}=1.14$–$1.31\,mm\,s^{-1}$) spin state both agree with the experimental value ($\delta=1.25(2)\,mm\,s^{-1}$). Unfortunately, comparison of the calculated quadrupole splitting for the high ($|\Delta E_Q{}^{calc}|=0.65$–$0.68\,mm\,s^{-1}$) and low ($|\Delta E_Q{}^{calc}|=2.01$–$2.36\,mm\,s^{-1}$) spin states to the experimental one ($\Delta E_Q=1.23(2)\,mm\,s^{-1}$) is not useful for determination of the spin state.

Electron paramagnetic resonance spectroscopy. To directly probe the spin ground states of **1**–**7**, we performed continuous-wave electron paramagnetic resonance (EPR) spectroscopy at the X-band (~9.4 GHz) and Q-band (~34 GHz) on polycrystalline samples. For brevity, we focus here on the data for **3** and **5**. The results of the remaining compounds are summarized, with a full analysis, in the Supplementary Information. We note that a continuous-wave X-band EPR spectrum of a frozen dichloromethane (DCM) solution of **3** at 100 K has been reported previously[28]. As expected for the $18e^-$ ferrocene analogue **2**, there is no EPR spectrum at any temperature at the X- or Q-band, in agreement with an $S=0$ ground state from CASSCF calculations. Similarly, the $18e^-$ **4** is also EPR-silent at X- and Q-band aside from signals arising from the presence of **1** (Supplementary Fig. 74). The X-band EPR spectrum at 5 K for **3** (Co^{2+}) shows a single feature around $g=1.89$ (Supplementary Fig. 72), suggesting a low-spin $S=1/2$ ground state, but a Q-band spectrum at 11 K reveals additional structure (Fig. 4a). Frozen solution experiments confirm an extrinsic peak in the powder spectrum at $g_{iso}=1.83$ (Supplementary Fig. 73), and simulations of the solid-state data with Easyspin[43] give $g_x=2.00$, $g_y=1.93$ and $g_z=1.72$ with hyperfine interaction with the ^{59}Co $I=7/2$ nuclear spin $A_x=400$, $A_y=0$ and $A_z=150$ MHz (Fig. 4a; we note that these hyperfine coupling constants are approximate due to the unresolved nature of the hyperfine structure).

The X-band EPR spectra of **5** between 5 and 20 K show a broad resonance between 0.1 and 0.3 T that increases in intensity with increasing temperature (Supplementary Fig. 75). Only a weak spectrum could be obtained at the Q-band (Fig. 4b), which shows a large positive feature at 0.5 T and a smaller negative feature at 1 T, suggestive of an easy-plane-like effective doublet state. Taken together with the temperature dependence of the X-band spectra, these results are consistent with an EPR-active excited state with easy-plane anisotropy. We hypothesize that this signal arises from an $S=3/2$ ground state with negative axial zero-field splitting ($D<0$) such that the ground $m_S=\pm3/2$ Kramers doublet (which would appear as easy-axis) is EPR-silent and the excited $m_S=\pm1/2$ doublet (which behaves as easy-plane) is EPR-active. Fitting the variable-temperature X-band and Q-band spectra simultaneously[44] gives $D=-4.42\,cm^{-1}$ with $E=0\,cm^{-1}$ and $g_{x/y}=2.06$ and $g_z=2.37$ (Fig. 4b and Supplementary Fig. 75), although we note that the magnitude of D is given solely by the temperature dependence of the X-band spectra, and is thus not spectroscopically determined and should be treated as an estimate.

Resonances in the Q-band EPR spectra of **5** are at different magnetic fields to those seen for **3** (Fig. 4), indicating different effective g values, which are far from $g=2$ for **5** (effective g values are $g_z=2.37$ and $g_{x/y}=4.12$). This provides a strong foundation for the assignment of **5** as arising from an $S=3/2$ spin state, in addition to the temperature dependence, as the large effective g values are very unlikely to arise from an $S=1/2$ system. Indeed, Rajasekharan et al. show that the g values for variously substituted low-spin d^7 mixed sandwich [(η^5-C_5R_5)Fe(η^6-C_6R_6)] complexes are between 1.2 and 2.1[45], consistent with our EPR data for **3** ($g_x=2.00$, $g_y=1.93$ and $g_z=1.72$) but clearly distinct from the data for **5** (effective g values of $g_z=2.37$ and $g_{x/y}=4.12$, arising from $S=3/2$, $D=-4.42\,cm^{-1}$ with $E=0\,cm^{-1}$ and $g_{x/y}=2.06$ and $g_z=2.37$). CASSCF-SO calculations agree well with the experimental data, predicting an axially anisotropic $S=1/2$ ground state for **3** with g values of $g_x\approx g_y=2.1$, $g_z=1.61$ and a ground $S=3/2$ spin state with negative uniaxial magnetic anisotropy for **5**; however, the experimental D value for **5** is far smaller than that calculated (−4.42 cf. $-36.4\,cm^{-1}$). Low g values <2 are unusual for greater-than-half-filled d-shell complexes such as **3** and [(η^5-C_5R_5)Fe(η^6-C_6R_6)][45], and arise from the low-spin configuration where a single unpaired electron resides in a near-degenerate pair of π^* orbitals (Fig. 5) where the orbital doublet degeneracy is lifted by low-symmetry perturbations, which has a parallel to the electronic structure and EPR spectra of d^3 Fe^{5+} nitrido and oxo complexes[46]. The negative D value for **5** in the high-spin ^4E ground state is a result of the uneven occupation of three electrons in the near-degenerate d_{xy/x^2-y^2} (δ symmetry) orbitals (Fig. 5) leading to a significant contribution of orbital angular

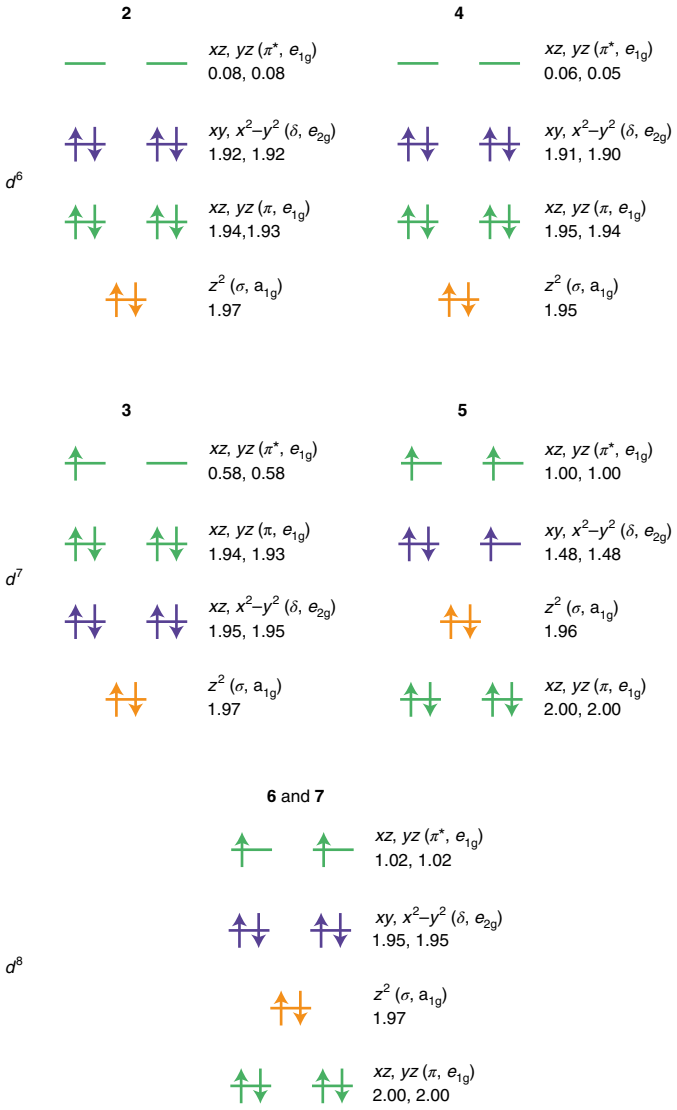

Fig. 5 | Orbital ordering, occupation and approximate symmetry labels for the active space of 2–7 from CASSCF-SO. The energy separation is not to scale and is merely indicative; visualized occupations are rounded (the occupations for **6** and **7** are identical and those shown for **2** are Fe1; those for Fe2 are nearly identical) and the five excited 4*d* orbitals are excluded. Note that each diagram has four electrons more than the formal d^n configuration, corresponding to the formally bonding π, e_{1g} electrons.

momentum along the *z* direction and domination of the D_{zz} component of the *D* tensor[47].

The difference in the ground spin states of **3** and **5** is probably a result of the compressed coordination sphere experienced by the metal in **3**, due to stronger dipolar interactions and shorter bond lengths for Co^{2+} (Table 1). This effect is analogous to that of high- and low-spin monomeric manganocenes[26]. Such changes in bonding clearly affect 3*d*-orbital energies, and it is commonplace to see orbital occupation diagrams of metallocenes from theoretical calculations. However, orbital energies are a single electron construct and thus are non-existent in a wavefunction where electron correlation is explicitly considered. Although we cannot produce orbital energy diagrams, we can use the state-averaged occupation of the active orbitals to infer their energetic ordering; that is, orbitals with greater occupation are lower in energy relative to those with lower occupation (Fig. 5). The orbital orderings for **2** and **4** are the same, but differ from the 'traditional' picture[48] of d_{xz}/d_{yz} (π, e_{1g}) < $d_{xy}/d_{x^2-y^2}$ (δ, e_{2g}) < d_{z^2} (σ, a_{1g}) < d_{xz}/d_{yz} (π^*, e_{1g}) (recently echoed by a DFT study[49]) and also from that determined with Hartree–Fock theory of d_{z^2} (σ, a_{1g}) < $d_{xy}/d_{x^2-y^2}$ (δ, e_{2g}) < d_{xz}/d_{yz} (π, e_{1g}) < d_{xz}/d_{yz} (π^*, e_{1g})[50]. The orbital orderings for **5**–**7** are the same as one another, yet differ from all other orderings already discussed, and are the same as that accepted for the ferrocenium cation[50]. Complex **3** is the clear outlier from our results here, where the d_{xz}/d_{yz} (π, e_{1g}) orbitals are the HOMO-1, and this ordering is in agreement with the Hartree–Fock results on ferrocene[50]. All of the occupation numbers (Supplementary Tables 8, 9, 11, 13, 15, 17 and 18) suggest that d_{z^2} (σ, a_{1g}) lies lower than the $d_{xy}/d_{x^2-y^2}$ pair (δ, e_{2g}), although for **2**–**4** and **6** and **7** the average occupations are quite close (1.97(1) and 1.93(2), respectively), so these orbitals may be quite close in energy; for **5** there is a much more significant difference in the occupation numbers of 1.96 and 1.48, respectively, clearly indicating that d_{z^2} is lower in energy than $d_{xy}/d_{x^2-y^2}$. The difference between this ordering and that of the 'traditional' picture must be due to electron correlation effects, but we reiterate that orbital energies do not exist in multi-reference wavefunctions such as those calculated here and so these orderings are only indicative.

The synthetic methodology presented herein should be transferable to other *d*-block metallocenates with appropriate functionalization. We note that these results come over 50 years after the first published efforts to reduce ferrocene with alkali metals[51]. In the first report of the electrochemical reduction of cobaltocene in 1974, Geiger predicted that metallocene anions would be interesting candidates to study electrophilic attack at metallocene centres[14]. Such reactivity studies on structurally authenticated ferrocene monoanions are now plausible. We envisage that the isolation of thermally stable examples will facilitate more rapid progress in this endeavour[21], as well as providing systems that are more amenable to magnetic and spectroscopic characterization.

Online content

Any methods, additional references, Nature Research reporting summaries, source data, extended data, supplementary information, acknowledgements, peer review information; details of author contributions and competing interests; and statements of data and code availability are available at https://doi.org/10.1038/s41557-020-00595-w.

Received: 11 May 2020; Accepted: 27 October 2020;
Published online: 14 December 2020

References

1. Kealy, T. J. & Pauson, P. L. A new type of organo-iron compound. *Nature* **168**, 1039–1040 (1951).
2. Miller, S. A., Tebboth, J. A. & Tremaine, J. F. 114. Dicyclopentadienyliron. *J. Chem. Soc.* **1952**, 632–635 (1952).
3. Wilkinson, G., Rosenblum, M., Whiting, M. C. & Woodward, R. B. The structure of iron bis-cyclopentadienyl. *J. Am. Chem. Soc.* **74**, 2125–2126 (1952).
4. Long, N. J. *Metallocenes—An Introduction to Sandwich Complexes* (Blackwell Science, 1998).
5. Togni, A. & Halterman, R. L. *Metallocenes: Synthesis Reactivity Applications* (Wiley, 1998).
6. Fukino, T. et al. Manipulation of discrete nanostructures by selective modulation of noncovalent forces. *Science* **344**, 499–540 (2014).
7. Astruc, D. Why is ferrocene so exceptional?. *Eur. J. Inorg. Chem.* **2017**, 6–29 (2017).
8. Jumde, R. P., Lanza, F., Veenstra, M. J. & Harutyunyan, S. R. Catalytic asymmetric addition of Grignard reagents to alkenyl-substituted aromatic N-heterocycles. *Science* **352**, 433–437 (2016).
9. Connelly, N. G. & Geiger, W. E. Jr Chemical redox agents for organometallic chemistry. *Chem. Rev.* **96**, 877–910 (1996).
10. Malischewski, M., Adelhardt, M., Sutter, J., Meyer, K. & Seppelt, K. Isolation and structural and electronic characterization of salts of the decamethylferrocene dication. *Science* **353**, 678–682 (2016).

11. Holloway, J. D. L., Bowden, W. L. & Geiger, W. E. Jr Unusual electron-transfer processes involving electron-rich and electron-deficient metallocenes. *J. Am. Chem. Soc.* **99**, 7089–7090 (1997).
12. Mugnier, Y., Moise, C., Tirouflet, J. & Laviron, E. Reduction electrochimique du ferrocene. *J. Organomet. Chem.* **186**, C49–C52 (1980).
13. Ito, N., Saji, T. & Aoyagui, S. Electrochemical formation of stable ferrocene anion and the formal rate constant of the ferrocene$^{0/-}$ electrode. *J. Organomet. Chem.* **247**, 301–305 (1983).
14. Geiger, W. E. Jr Electroreduction of cobaltocene. Evidence for a metallocene anion. *J. Am. Chem. Soc.* **96**, 2632–2634 (1974).
15. Bard, A. J., Garcia, E., Kukharenko, S. & Strelets, V. V. Electrochemistry of metallocenes at very negative and very positive potentials. Electrogeneration of 17-electron Cp_2Co^{2+}, 21-electron Cp_2Co^{2-}, and 22-electron Cp_2Ni^{2-} species. *Inorg. Chem.* **32**, 3528–3531 (1993).
16. Smart, J. C. & Robbins, J. L. A low spin manganocene and its novel anionic derivative. Synthesis and characterization of decamethylmanganocene complexes. *J. Am. Chem. Soc.* **100**, 3936–3937 (1978).
17. Robbins, J. L., Edelstein, N. M., Cooper, S. R. & Smart, J. C. Syntheses and electronic structures of decamethylmanganocenes. *J. Am. Chem. Soc.* **101**, 3853–3857 (1979).
18. Baudry, D. & Ephritikhine, M. Reactions de $(\eta^5\text{-}C_5H_5)_2$reh et de ses derives. Preparation de nouveaux complexes biscyclopentadienyles du rhenium. *J. Organomet. Chem.* **195**, 213–222 (1980).
19. Gardner, B. M., McMaster, J., Lewis, W. & Liddle, S. T. Synthesis and structure of $[\{N(CH_2CH_2NSiMe_3)_3\}URe(\eta^5\text{-}C_5H_5)_2]$: a heterobimetallic complex with an unsupported uranium-rhenium bond. *Chem. Commun.* **2009**, 2851–2853 (2009).
20. Hung-Low, F. & Bradley, C. A. Synthesis of a bis(indenyl) Co(I) anion: a reactive source of a 14 electron indenyl Co(I) equivalent. *Inorg. Chem.* **52**, 2446–2457 (2013).
21. Malischewski, M. & Seppelt, K. Structural characterization of potassium salts of the decamethylmanganocene anion $Cp^*_2Mn^-$. *Dalton Trans.* **48**, 17078–17082 (2019).
22. Astruc, D., Román, E., Hamon, E., Batail, J. R. & Novel, P. Reactions of dioxygen in organometallic chemistry. Hydrogen atom abstraction vs. dimerization of the 19-electron complexes η^5-cyclopentadienyliron(I) η^6-arene. *J. Am. Chem. Soc.* **101**, 2240–2242 (1979).
23. Hamon, J. R., Astruc, D. & Michaud, P. Syntheses, characterizations, and stereoelectronic stabilization of organometallic electron reservoirs: the 19-electron d^7 redox catalysts $\eta^5\text{-}C_5R_5Fe\text{-}\eta^6\text{-}C_6R'_6$. *J. Am. Chem. Soc.* **103**, 758–766 (1981).
24. Saito, M. et al. Anionic stannaferrocene and its unique electronic state. *Chem. Lett.* **48**, 163–165 (2019).
25. Sitzmann, H., Schär, M., Dormann, E. & Kelemen, M. High spin-manganocenes with bulky, alkylated cyclopentadienyl ligands. *Z. Anorg. Allg. Chem.* **623**, 1609–1613 (1997).
26. Walter, M. D., Sofield, C. D., Booth, C. H. & Andersen, R. A. Spin equilibria in monomeric manganocenes: solid-state magnetic and EXAFS studies. *Organometallics* **28**, 2005–2019 (2009).
27. Walter, M. D. & White, P. S. $[Cp'FeI]_2$ as convenient entry into iron-modified pincer complexes: bimetallic η^6,κ^1-POCOP-pincer iron iridium compounds. *New J. Chem.* **35**, 1842–1854 (2011).
28. Schneider, J. J. et al. Synthesis, structure and spectroelectrochemistry of bis(η^6-1,4-tri-*tert*-butyl-benzene)chromium(0) and bis(η^5-1,2,4-tri-*tert*-butyl-cyclopentadienyl)cobalt(II). Dia- and paramagnetic sandwich complexes derived from sterically highly demanding π-ligands. *J. Organomet. Chem.* **590**, 7–14 (1999).
29. Peters, M. et al. Pogo-stick iron and cobalt complexes: synthesis, structures, and magnetic properties. *Inorg. Chem.* **58**, 16475–16486 (2019).
30. Jaroschik, F., Nief, F., Le Goff, X.-F. & Ricard, L. Synthesis and reactivity of organometallic complexes of divalent thulium with cyclopentadienyl and phospholyl ligands. *Organometallics* **26**, 3552–3558 (2007).
31. Woen, D. H. & Evans, W. J. in *Handbook on the Physics and Chemistry of Rare Earths* Vol. 50 (eds Bünzli, J.-C. G. & Pecharsky, V. K.) Ch. 293, 337–394 (Elsevier, 2016).
32. Fischer, E. O. & Leipfinger, H. Weitere magnetische Untersuchungen zur Struktur der cyclopentadien- und inden-Verbindungen der Übergangsmetalle. *Z. Naturforsch.* **10b**, 353–355 (1955).
33. Wilkinson, G., Cotton, F. A. & Birmingham, J. M. On manganese cyclopentadienide and some chemical reactions of neutral bis-cyclopentadienyl metal compounds. *J. Inorg. Nucl. Chem.* **2**, 95–113 (1956).
34. Walter, M. D., Sofield, C. D. & Andersen, R. A. Spin equilibria and thermodynamic constants for $(C_5H_4R)_2Mn$, R = H or Me, in solid solutions of diamagnetic diluents. *J. Organomet. Chem.* **776**, 17–22 (2015).
35. Switzer, M. E., Wang, R., Rettig, M. F. & Maki, A. H. Electronic ground states of manganocene and 1,1′-dimethylmanganocene. *J. Am. Chem. Soc.* **96**, 7669–7674 (1974).
36. Fdez. Galván, I. et al. OpenMolcas: from source code to insight. *J. Chem. Theory Comput.* **15**, 5925–5964 (2019).
37. Wickman, H. H., Klein, M. P. & Shirley, D. A. Paramagnetic hyperfine structure and relaxation effects in Mössbauer spectra: Fe^{57} in ferrichrome *A*. *Phys. Rev.* **152**, 345 (1966).
38. Stoian, S. A. et al. Mössbauer, electron paramagnetic resonance, and crystallographic characterization of a high-spin Fe(I) diketiminate complex with orbital degeneracy. *Inorg. Chem.* **44**, 4915–4922 (2005).
39. Wertheim, G. K. & Herber, R. H. Fe^{57} Mössbauer effect in ferrocene derivatives. *J. Chem. Phys.* **38**, 2106–2111 (1963).
40. Stukan, R. A., Gubin, S. P., Nesmeyanov, A. N., Gol'danskii, V. I. & Makarov, E. F. A Mössbauer study of some ferrocene derivatives. *Theor. Exper. Chem.* **2**, 581–584 (1966).
41. Reiners, M. et al. Study on spin–lattice relaxation processes in *tert*-butyl substituted ferrocenium derivatives. *Eur. J. Inorg. Chem.* 388–400 (2017).
42. Mariot, J. P. et al. Mössbauer study and molecular orbital calculations on the organo-iron(I, II) electron reservoir sandwiches CpFen+ $(\eta^6\text{-}C_6(CH_3)_6)$ (n = 0,1) and related CpFe (cyclohexadienyl) complexes. *J. Physique* **44**, 1377–1385 (1983).
43. Stoll, S. & Schweiger, A. EasySpin, a comprehensive software package for spectral simulation and analysis in EPR. *J. Magn. Reson.* **178**, 42–55 (2006).
44. Chilton, N. F., Anderson, R. P., Turner, L. D., Soncini, A. & Murray, K. S. PHI: a powerful new program for the analysis of anisotropic monomeric and exchange-coupled polynuclear *d*- and *f*-block complexes. *J. Comput. Chem.* **34**, 1164–1175 (2013).
45. Rajasekharan, M. V. et al. EPR studies of the electronic structure and dynamic Jahn–Teller effect in iron(I) sandwich compounds. *J. Am. Chem. Soc.* **104**, 2400–2407 (1982).
46. Chang, H.-C. et al. Electron paramagnetic resonance signature of tetragonal low spin iron(V)–nitrido and –oxo complexes derived from the electronic structure analysis of heme and non-heme archetypes. *J. Am. Chem. Soc.* **141**, 2421–2434 (2019).
47. Gomez-Coca, S., Cremades, E., Aliaga-Alcalde, N. & Ruiz, E. Mononuclear single-molecule magnets: tailoring the magnetic anisotropy of first-row transition–metal complexes. *J. Am. Chem. Soc.* **135**, 7010–7018 (2013).
48. Molloy, K. C. (ed.) in *Group Theory for Chemists* 2nd edn, Ch. 10, 109–118 (Woodhead Publishing, 2013); https://doi.org/10.1533/9780857092410.3.109
49. Cirera, J. & Ruiz, E. Electronic and steric control of the spin-crossover behavior in $[(Cp^R)_2Mn]$ manganocenes. *Inorg. Chem.* **57**, 702–709 (2018).
50. Ishimura, K., Hada, M. & Nakatsuji, H. Ionized and excited states of ferrocene: symmetry adapted cluster–configuration–interaction study. *J. Chem. Phys.* **117**, 6533–6537 (2002).
51. Watt, G. W. & Baye, L. J. Reactions of metallocenes with potassium and potassium amide in liquid ammonia. *J. Inorg. Nucl. Chem.* **26**, 2099–2102 (1964).

Methods

General procedures. All manipulations were performed using standard Schlenk techniques or in an Inert Purelab HE 2GB glovebox. Solvents were dried by passing through columns containing activated alumina and molecular sieves or by refluxing over potassium followed by distillation, and were degassed before use. Complexes were variously characterized by cyclic voltammetry, single-crystal XRD (a Rigaku XtalLAB AFC11 or Rigaku Oxford Diffraction SuperNova diffractometer equipped with charge-coupled device area detectors), elemental microanalysis, NMR, EPR, Fourier-transform infrared (FTIR), Raman and UV–vis–NIR spectroscopies, and DFT and CASSCF calculations. Complexes **2** and **5** were additionally studied by ^{57}Fe Mössbauer spectroscopy. [$(Cp^{ttt})_2M$] (**1**–**3**) were prepared by salt metathesis protocols from the parent MCl_2 and 2 equiv. of KCp^{ttt} in THF under reflux conditions, and were isolated by removal of volatiles in vacuo followed by recrystallization from hexane, by adapting published procedures[25–27,29]. [K(2.2.2-crypt)][$(Cp^{ttt})_2M$] (**4**–**6**) were prepared by reduction of the parent **1**–**3** with KC_8 (ref. [52]) in the presence of 2.2.2-cryptand in THF at −40 °C, and were isolated by filtration and layering with hexane at −40 °C. The following sections provide example syntheses of **3** and **5**.

Synthesis of [$(Cp^{ttt})_2Co$] (3). THF (20 ml) was added to a pre-cooled (−78 °C) mixture of $CoCl_2$ (0.390 g, 3.0 mmol) and KCp^{ttt} (1.635 g, 6.0 mmol) in a grease-free Teflon stoppered vessel (Rotaflo), then allowed to warm slowly to room temperature. As the mixture warmed, the solution slowly turned dark brown. The mixture was heated at 80 °C for 16 h, which produced dark brown solution with a pale precipitate. The mixture was cooled and the volatiles were removed in vacuo to afford a brown solid. Hexane (30 ml) was added, and the mixture heated at 80 °C for 3 h, cooled to room temperature and filtered away from pale solids. The solution was concentrated to ~1.5 ml and stored at 5 °C for 16 h, giving **3**·(C_6H_{14}) as large brown plates (1.076 g, 59%). Anal. Calcd (%) for $C_{34}H_{58}Co{\cdot}C_6H_{14}$: C, 78.51; H, 11.86. Found: C, 79.36; H, 11.82. ^{1}H NMR (C_6D_6, 400 or 500 MHz, 298 K): δ = 3.50 (br. s), 3.67 (br. s). ^{13}C{^{1}H} NMR (C_6D_6, 125 MHz). No peaks were observed. FTIR (ATR, microcrystalline): $\tilde{\nu}$ = 402 (w), 424 (w), 436 (w), 453 (w), 477 (w), 494 (w), 504 (w), 524 (m), 538 (w), 549 (w), 565 (w), 598 (m), 612 (w), 620 (w), 632 (w), 640 (w), 659 (w), 675 (w), 693 (w), 702 (w), 708 (w), 718 (w), 724 (w), 742 (w), 753 (w), 777 (w), 791 (w), 826 (w), 842 (w), 850 (w), 873 (w), 885 (w), 904 (w), 916 (w), 926 (w), 948 (w), 977 (w), 1,003 (w), 1,016 (w), 1,056 (m), 1,065 (m), 1,073 (m), 1,097 (m), 1,128 (m), 1,152 (w), 1,163 (w), 1,173 (w), 1,201 (m), 1,234 (s), 1,260 (s), 1,275 (m), 1,297 (s), 1,328 (m), 1,354 (vs), 1,387 (s), 1,409 (m), 1,446 (m), 1,458 (m), 1,477 (s), 1,511 (m), 1,540 (m), 1,575 (m), 1,589 (m), 1,617 (w), 1,634 (w), 1,674 (w), 1,699 (m), 1,732 (w), 1,758 (w), 1,781 (m), 1,819 (m), 1,858 (m), 1,882 (m), 1,891 (m), 1,909 (m), 1,938 (m), 1,962 (m), 1,976 (s), 2,009 (s), 2,033 (m), 2,048 (m), 2,072 (m), 2,131 (w), 2,148 (m), 2,156 (m), 2,254 (m), 3,016 (s). ^{1}H NMR spectroscopy was in agreement with earlier reports[28,29].

Synthesis of [K(2.2.2-crypt)][$(Cp^{ttt})_2Fe$] (5). THF (2 ml) was added to a mixture of **2** (0.366 g, 0.7 mmol) and 2.2.2-cryptand (0.264 g, 0.7 mmol) to give a bright ruby-red solution. This solution was added rapidly to a pre-cooled (−78 °C) Schlenk vessel containing KC_8 (0.095 g, 0.7 mmol) and a Teflon-coated stirrer bar. The slurry was stirred rapidly and allowed to warm to −40 °C over the course of 10 min, during which time the colour changed from ruby red to dark brown. The mixture was stirred at −40 °C for 10 min, then allowed to settle for a further 5 min. The brown solution was filtered cold to a pre-cooled (−40 °C) vessel, and concentrated at this temperature to ~1 ml. Hexane (4 ml) was carefully layered on top, which caused some crystals to immediately form. The vessel and cold bath were transferred to a freezer (−25 °C) to warm slowly to −25 °C overnight. Brown blocks of **5** were isolated by cold filtration (0.140 g, 21%). Anal. Calcd (%) for $C_{52}H_{94}O_6N_2KFe$: C, 66.57; H, 10.10; N, 2.99. Found: C, 66.60; H, 10.47; N, 3.03. ^{1}H NMR (C_4D_8O, 400 MHz, 298 K): δ = −8.12 (s, 18H, FWHM = 186 Hz, $C_5H_2(CMe_3)$), −2.70 (s, 36H, FWHM = 423 Hz, $(C_5H_2(CMe_3)_2)$), 2.28–2.78 (36H, 2.2.2-cryptand), Cp^{ttt}-C*H* not observed. ^{13}C{^{1}H} NMR (C_4D_8O, 125 MHz) 35.76, 55.45, 57.43, 69.59, 70.51, 71.85, 72.96, 126.19, 127.00. FTIR (ATR, microcrystalline): $\tilde{\nu}$ = 406 (m), 414 (w), 428 (m), 447 (w), 459 (w), 467 (w), 483 (w), 524 (m), 563 (m), 591 (w), 661 (w), 667 (w), 753 (m), 777 (m), 791 (m), 832 (m), 850 (w), 930 (m), 950 (s), 983 (m), 995 (m), 1,026 (m), 1,077 (s), 1,085 (s), 1,103 (vs), 1,132 (s), 1,195 (w), 1,234 (m), 1,260 (m), 1,275 (w), 1,295 (m), 1,328 (w), 1,352 (m), 1,385 (m), 1,446 (m), 1,458 (m), 1,477 (m), 1,509 (w), 1,542 (w), 1,575 (w), 1,591 (w), 1,630 (w), 1,644 (w), 1,674 (w), 1,699 (w), 1,719 (w), 1,734 (w), 1,754 (w), 1,781 (w), 1,791 (w), 1,821 (w), 1,836 (w), 1,852 (w), 1,878 (w), 1,895 (w), 1,905 (w), 1,915 (w), 1,938 (w), 1,962 (w), 1,978 (w), 2,009 (w), 2,035 (w), 2,046 (w), 2,068 (w), 2,164 (w), 2,168 (w), 2,239 (w), 2,280 (w), 2,317 (m), 2,341 (w), 2,372 (w), 2,815 (m), 2,882 (m), 2,949 (m), 3,018 (w), 3,049 (w), 3,059 (w), 3,067 (w), 3,076 (w), 3,086 (w), 3,096 (w), 3,104 (w), 3,114 (w), 3,123 (w).

Electrochemistry. All electrochemistry experiments were initially assessed at the open-circuit potential and redox potentials are referenced to the $FcH^{+/0}$ couple (unless otherwise stated), which was used as an internal standard. Cyclic voltammetry was carried out using a sealed cell and a three-electrode arrangement, with a Pt wire working electrode, Pt flag secondary electrode and an AgCl/Ag wire pseudo-reference electrode prepared by soaking a Ag wire in $FeCl_{3(aq)}$ before rinsing with water and acetone. Where measurements were performed at low temperature, the cell was equilibrated back to room temperature after each scan and stirred thoroughly before cooling in a −50 °C acetone/liquid nitrogen bath without stirring (at least 1 min to equilibrate) then transferred back into the Faraday cage and measurements performed promptly to minimize warming.

CASSCF calculations. OpenMolcas v18.09 was used for all calculations[36], employing the unoptimized XRD structure of each complex, with counterions and/or solvent removed, and include a sphere of point charges (+2 for M^{2+}, +1 for M^{1+}, −0.2 for Cp-ring carbon atoms, +1 for K^+ counterions) of 40-Å radius to model the crystalline electric potential. Basis functions for all atoms are from the ANO-RCC library[53,54], using valence triple zeta polarised (VTZP) quality for the 3*d* metal atom, valence double zeta polarised (VDZP) quality for the 10 Cp-ring carbon atoms, and valence double zeta (VDZ) quality for all other atoms. We use the second-order Douglas–Kroll–Hess (DKH) transformation for the relativistic Hamiltonian and Cholesky decomposition with a threshold of 10^{-8} for the two-electron integrals. We start with an active space of five 3*d* orbitals (nominally $3d_{z^2}$ (σ, a_{1g}), $3d_{xy}$ and $3d_{x^2-y^2}$ (δ, e_{2g}), and $3d_{xz}$ and $3d_{yz}$ (π^*, e_{1g})), and use the restricted active space (RAS) probing method[55] to locate two bonding 3*d* ($3d_{xz}$ and $3d_{yz}$ (π, e_{1g})) and five excited 4*d* orbitals to include them in the active space, and subsequently optimize the orbitals using SA-CASSCF for all states below ~40,000 cm^{-1} for each spin multiplicity (relative energies). Then, we re-optimize the orbitals by considering only the lowest-lying well-isolated states for each multiplicity. In the last step, we perform a configuration interaction expansion in the optimized active space to find roots that are below 30,000 cm^{-1} for each spin multiplicity (relative energies), and then mix all states with SOC.

Mössbauer spectroscopy. Spectra were recorded at 80 K in zero applied field using a constant acceleration spectrometer and a ^{57}Co/Rh source. The samples used for these measurements consisted of ground powders of **2** and **5** that were contained in polyether ether ketone sample cups with tightly fitted lids. The isomer shift is reported relative to that of α-Fe at room temperature. Spectral simulations were generated using the WMOSS software package (SEE Co.).

EPR spectroscopy. EPR samples were prepared as ground powders and flame-sealed under an inert atmosphere while keeping the sample at 77 K in 2-mm Q-band and 4-mm X-band tubes. A frozen solution sample of **3** was prepared at 5 mM concentration in a mixed 9:1 toluene:*n*-hexane solvent system. The solution sample was frozen in liquid nitrogen then loaded into the spectrometer. Spectra were collected using Bruker EMX300 and E500 spectrometers. Low-temperature measurements were achieved using liquid helium cooling to 5 K. A strong pitch standard of g = 2.0028 was used to calibrate the magnetic field.

Data availability

Crystallographic data for the structures reported in this Article have been deposited at the Cambridge Crystallographic Data Centre, under deposition nos. CCDC 1951767 (**1**), 1951768 (**2**), 1951769 (**3**), 1951770 (**4**), 1951771 (**5**), 1951772 (**6**), 1951773 (**7**) and 1951774 (**8**). Copies of the data can be obtained free of charge from the CCDC via www.ccdc.cam.ac.uk/structures. Raw research data files supporting this publication are available from Mendeley Data at https://doi.org/10.17632/rzzpcwgkx5.1. Apart from the datasets mentioned, all other data supporting the findings of this study are available within the Article and Supplementary Information.

References

52. Bergbreiter, D. E. & Killough, J. M. Reactions of potassium-graphite. *J. Am. Chem. Soc.* **100**, 2126–2134 (1978).
53. Roos, B. O., Lindh, R., Malmqvist, P.-Å., Veryazov, V. & Widmark, P.-O. Main group atoms and dimers studied with a new relativistic ANO basis set. *J. Phys. Chem. A* **108**, 2851–2858 (2004).
54. Roos, B. O., Lindh, R., Malmqvist, P.-Å., Veryazov, V. & Widmark, P.-O. New relativistic ANO basis sets for transition metal atoms. *J. Phys. Chem. A* **109**, 6575–6579 (2005).
55. Veryazov, V., Malmqvist, P. Å. & Roos, B. O. How to select active space for multiconfigurational quantum chemistry? *Int. J. Quant. Chem.* **111**, 3329–3338 (2011).

Acknowledgements

We acknowledge funding from the Engineering and Physical Sciences Research Council (Doctoral Prize Fellowship to C.A.P.G., EP/N007034/1 for M.V., EP/R002605X/1 for P.E., studentship for H.M.N. and EP/K039547/1 for a single-crystal X-ray diffractometer), the Royal Society (University Research Fellowship to N.F.C.), European Research Council CoG-816268 (D.P.M. and M.J.G.) and StG-851504 (N.F.C.) and the University of Manchester (Presidential Doctoral Prize to M.J.G.). C.A.P.G. and S.M.G. thank the Laboratory Directed Research and Development (LDRD) programme at Los Alamos National Laboratory (an affirmative action/equal opportunity employer, managed by Triad National Security, LLC, for the NNSA of the US Department of Energy) (contract

no. 89233218CNA000001) for a distinguished J. Robert Oppenheimer Postdoctoral Fellowship and Directors Fellowship, respectively. S.H. acknowledges support from the National Science Foundation (DMR-1610226). We thank the EPSRC UK National Electron Paramagnetic Resonance Service for access to the EPR Facility, and the University of Manchester for access to the Computational Shared Facility. A portion of this work was performed at the National High Magnetic Field Laboratory, which is supported by the National Science Foundation Cooperative agreement no. DMR-1644779 and the State of Florida. We also thank F. Ortu for assistance with the collection of Raman spectra. This project has received funding from the European Research Council (ERC) under the European Union's Horizon 2020 research and innovation programme (grant agreements nos. 816268 and 851504).

Author contributions

C.A.P.G. and D.P.M. provided the original concept. C.A.P.G. synthesized and characterized the compounds. H.M.N. and P.E. carried out supporting synthetic and characterization work. D.P.M. supervised the synthetic component. M.J.G., M.V. and N.F.C. collected and interpreted EPR data. M.V. and N.F.C. performed CASSCF calculations. N.F.C. supervised the EPR and CASSCF components. S.M.G. collected and interpreted Mössbauer spectra and performed DFT calculations. S.H. supervised S.M.G. and provided additional EPR/Mössbauer interpretation. D.P.M. and N.F.C. wrote the manuscript, with contributions from all authors.

Competing interests

The authors declare no competing interests.

Additional information

Supplementary information is available for this paper at https://doi.org/10.1038/s41557-020-00595-w.

Correspondence and requests for materials should be addressed to N.F.C. or D.P.M.

Reprints and permissions information is available at www.nature.com/reprints.